Autonomous Synergic Control of Nanomotors
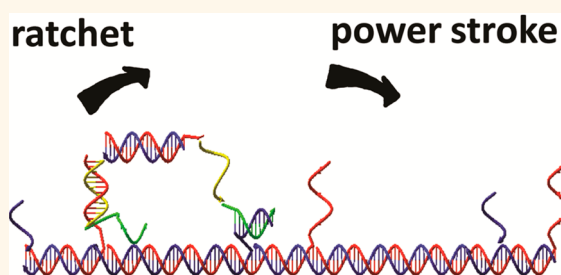
Meihan Liu,[†,#] Ruizheng Hou,[†,§,#] Juan Cheng,[†,#] Iong Ying Loh,[†] Sarangapani Sreelatha,[†] Ju Nie Tey,[⊥] Jun Wei,[⊥] and Zhisong Wang[†,‡,§,*]

[†]Department of Physics, [‡]NUS Graduate School for Integrative Sciences and Engineering, and [§]Center for Computational Science and Engineering, National University of Singapore, Singapore 117542 and [⊥]Singapore Institute of Manufacturing Technology, 71 Nanyang Drive, Singapore 638075. [#]M. Liu, R. Hou, and J. Cheng contributed equally to this study.

ABSTRACT Control is a hallmark of machines; effective control over a nanoscale system is necessary to turn it into a nanomachine. Nanomotors from biology often integrate a ratchet-like passive control and a power-stroke-like active control, and this synergic active-plus-passive control is critical to efficient utilization of energy. It remains a challenge to integrate the two differing types of control in rationally designed nanomotor systems. Recently a light-powered track-walking DNA nanomotor was developed from a bioinspired design principle that has the potential to integrate both controls. However, it is difficult to separate experimental signals for either control due to a tight coupling of both controls. Here we present a systematic study of the motor and new derivatives using different fluorescence labeling schemes and light operations. The experimental data suggest that the motor achieves the two controls autonomously through a mechanics-mediated symmetry breaking. This study presents an experimental validation for the bioinspired design principle of mechanical breaking of symmetry for synergic ratchet-plus-power stroke control. Augmented by mechanical and kinetic modeling, this experimental study provides mechanistic insights that may help advance molecular control in future nanotechnological systems.

KEYWORDS: nanomotor · DNA · control · kinesin · myosin · optomechanics

The past decade has seen thriving multidisciplinary endeavors to turn single molecules into a machine that converts externally supplied energy into directional mechanical outputs such as force generation, translation, and rotation. Experimental success covers molecular shuttles[1−4] and rotors[5−8] in a localized setup, molecular walkers[9−20] running on open tracks, and larger systems that incorporated these "engines" for nanotechnological applications.[21−24] The systems implementing these machines range from synthetic supramolecular compounds and engineered biomolecules in aqueous environments to small molecules[25] on solid-state surfaces. The methods of energy supply include chemical fuels, fuels plus enzymes,[11−13] light irradiation,[2−5,19,20] and electric currents from a scanning tunneling microscope tip.[25] Despite differing molecular systems and operational methods, these molecular machines, and more to come in the future, must address the same core challenge of controlling individual constituent molecules so as to rectify directional outputs of a machine as a whole. The better the control, the better the machine.

Two basic concepts of molecular control have been identified. One is a passive, ratchet-like control[26−32] that rectifies a machine's output toward a chosen direction by blocking stochastic molecular transitions conducive to the oppositely directed output. The other is an active, power-stroke-like control[8,27,29−31,33−35] in which energy consumption directly drives the forward output as an energetically downhill transition. As far as nanomotors are concerned, either ratchet or power stroke is able to rectify a net directional stepping in an average sense. But the chance of either control alone making a successful forward step per event of energy consumption or per fuel molecule consumed is subject to a fundamental upper limit of 50%, as a recent theoretical study[36] suggests. Breaking the limit is necessary for a nanomotor's efficient utilization of energy, and a viable route[36] is integration of ratchet and power stroke. Indeed, two biological nanomotors, F1-ATPase rotor and kinesin

walker, are known to integrate[27,30,32,34,36] both controls to achieve more than 99% fidelity[37−42] of forward stepping per fuel molecule consumed, a trait underlying efficient[43,44] utilization of fuel energy by both motors.

The detailed mechanisms of biological nanomotors attaining the synergic control of passive ratchet plus active stroke remain largely unclear due to complexity of the biological systems. Artificial nanomotors reported to date mostly implemented the ratchet,[11−16,19,45−47] and many adopted a burn-the-bridge method.[11−13,15,19] It remains a challenge to integrate the two differing types of control in a rationally designed motor−track system without modifying its irreversibly. Recently a track-walking bipedal DNA nanomotor[20] powered by light was developed from a bioinspired design principle[31] that has the potential to implement both controls simultaneously. However, it is difficult to obtain direct experimental signals for either control separately, partly due to a tight coupling of the two controls. In this paper, we carry out a systematic study of the motor and new variations using different molecular constructions, fluorescence labeling schemes, and light operations. The experimental data plus a mechanical−kinetic modeling are used to analyze mechanistic integration of the motors.

RESULTS

Motor-Track Systems. As illustrated in Figure 1, the motor is a ∼6.8 nm long DNA double-strand helix (D3−D3*, two helical turns) connecting two identical single-strand legs. Either leg is a 20-nucleotide-long D2 segment followed by a 5-nucleotide-long D1 segment plus D2. For mechanical flexibility, a 4-nucleotide long single-strand linker (S1) is introduced at the junction of the leg and the D3−D3* helix. The track is made of periodic double-strand helices D4−D4* (25.5 nm long) and D5−D5* (5.1 nm), which supports repeated pairs of D1* and D2*overhangs between the helices.

A leg of the motor binds to the track by forming double-strand helices with either a D1* or D2* foothold. The ensuing D1−D1* and D2−D2* helices are ∼1.7 and ∼6.8 nm long, respectively. Each pair of D1* and D2* footfolds sandwiching a D5−D5* helix may be regarded as a composite binding site, since it is the only track domain capable of forming thermodynamically stable helices with the motor's legs. Drawing from the D1* to D2* within a composite site points to a unique end of the track, which will be called the plus end hereafter.

The motor can be operated through any technical means that breaks the D2−D2* helix without destabilizing the chemically different D1−D1* duplex. We develop a light-powered version in which the leg's D2 segment contains light-responsive azobenzene moieties[48] in the nucleotide backbone. The operation is achieved by alternate irradiation of UV and visible
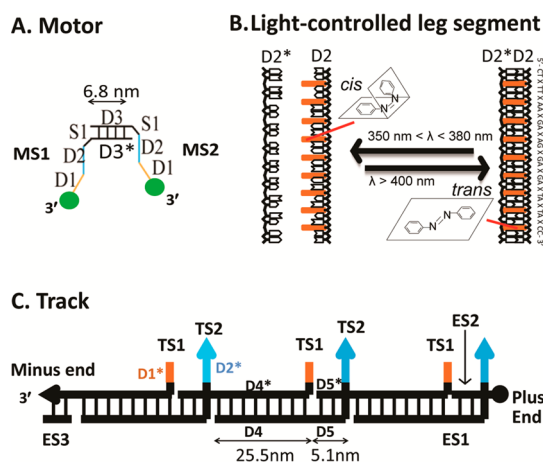

Figure 1. Schematic illustration of the motor−track construction. The motor is made of two DNA strands (MS1, MS2) and has two identical single-strand legs with sequences D1−D2. The track is made of five species of DNA strands (TS1, TS2, ES1, ES2, and ES3) and supports three binding sites that are each formed by two adjacent single-strand overhangs D1* and D2* (stars indicate complementary sequences). A truncated two-site track with the middle TS1 and TS2 strands removed is also used in this study. The motor carries a light-emitting dye (FAM, shown as a green sphere in panel A) at either leg, and the track's plus end carries a quencher (IBRQ, shown as a black sphere in panel C). Panel B illustrates the azo-tethered leg segment (D2) and its light-controlled hybridization with the complementary D2* segment from the track. Also shown are the cis and trans configurations of the azobenzene moieties (represented by long rectangles and marked as "X" in the given ncuelotide sequence for D2).

light: Light absorption by the azo-moieties in the UV creates a high-energy cis form that breaks the D2−D2* duplex; visible light absorption returns the moieties to the ground-state trans form that maintains a stable D2−D2* duplex.

For the sake of motor motility measurement, the motor was labeled with two light-emitting dye molecules (FAM, excitation/emission wavelength as 495/520 nm) at the 5′ ends of the legs. The track's plus end was labeled with a quencher (Iowa Black RQ) so as to reduce the fluorescence emission of a motor upon its arrival at the plus end.

In the present study, we also fabricate and test two new motor variations and redesign the track for site-specific labeling of two different dyes to yield more details of the motor's operation. The two motor variations are obtained by making their D3−D3* duplex one or two helical turns longer than the previous motor (called normal motor hereafter).

Design Principle. The motors are an implementation of a design principle[31] that is inspired by biomotors.[30,49] A key character of this bioinspired design principle is that a motor of symmetric legs may gain a net direction from proper free-energy gaps between motor−track binding states of differing geometric features. As schematically illustrated in Figure 2, a motor of the present study has four possible intersite

bridge states in which the motor's two legs are bound to two adjacent composite sites. Two are symmetric in that the motor's two legs hybridize into identical helices with the track (*i.e.*, states B2 and B3 in Figure 2). The other two are reversely asymmetric; the D1—D1* helix leads the D2—D2* toward the plus end in one state (B1) and toward the opposite end in the other (B4). If the motor's B1 state has a lower free energy and thereby occurs more often than B4 by Boltzmann's law, the symmetry of motor—track binding is broken in the sense that the leg to the plus end (referred to as leading leg hereafter) is in the D1—D1* helix and the trailing leg is in D2—D2*.

For a motor initially in the B1 state, as shown in Figure 3A, the UV irradiation has a chance to dissociate the trailing leg off the track but not the leading leg, though both are chemically identical. This position-selective dissociation of the rear leg is a Brownian ratchet effect. The leg dissociation triggers a migration of the front leg from the D1* foothold to the nearby D2* to form a longer, *i.e.*, more stable, helix. The visible

light irradiation stabilizes this intrasite downhill migration, which places the dissociated leg closer to the forward composite site than to the backward site. Thus the dissociated leg is biased to bind the forward site under visible light to resume the stable B1 state at a location one step forward. The migration-induced bias for forward binding is a power stroke.

There must exist a regime of small size of the motor where the B1 state becomes the lowest in free energy among the intersite bridge states, as suggested by a qualitative analysis.[20] This conclusion is supported by a simplistic mechanical model for the DNA motor. Figure 2 shows the free energies for the four bridge states predicted by the mechanical model *versus* the motor's size as the latter is hypothetically changed by assuming a different length for the D3—D3* duplex. When the duplex is long, *e.g.*, more than five helical turns, the B4 and B1 states are almost equal in free energy, and the symmetric B3 state is even lower. When the D3—D3* duplex becomes short, *e.g.*, two helical turns as for the motor, the free energies for B4 and B3 are elevated beyond that for B1, rendering it the most accessible bridge state. Qualitatively speaking, the trend of size dependence is meaningful and largely decided by geometry of the states, despite the limited power of the mechanical model for quantitative prediction (see below for the reasons). Overall, the model predicts that the symmetry breaking exists in the motors but deteriorates for the elongated motor variations. This size dependence is a character of the design principle.

Light-Driven Directional Motility of the Motor. Two sets of motility experiments and one set of control experiments were done using the same amount of motor sample. The motor is quencher-labeled, and the tracks are dye-labeled (Figure 1). The two sets of motility experiments both used an equimolar motor—track mix but respectively for a track containing two composite binding sites and for a track containing three sites. Before the light operation was applied, the
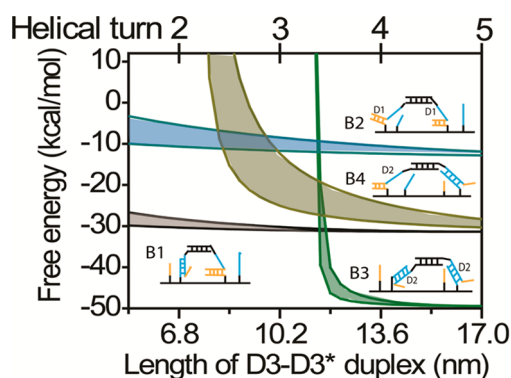

Figure 2. Free energies of the motor's bridge states predicted by a simplistic mechanical model *versus* length of the motor's D3—D3* duplex. The shadows indicate the upper and lower boundary due to uncertainty of the persistence length for single-stranded DNA (between 1—3 nm from ref 54). The zero value for free energies corresponds to the motor with both legs derailed off the track.
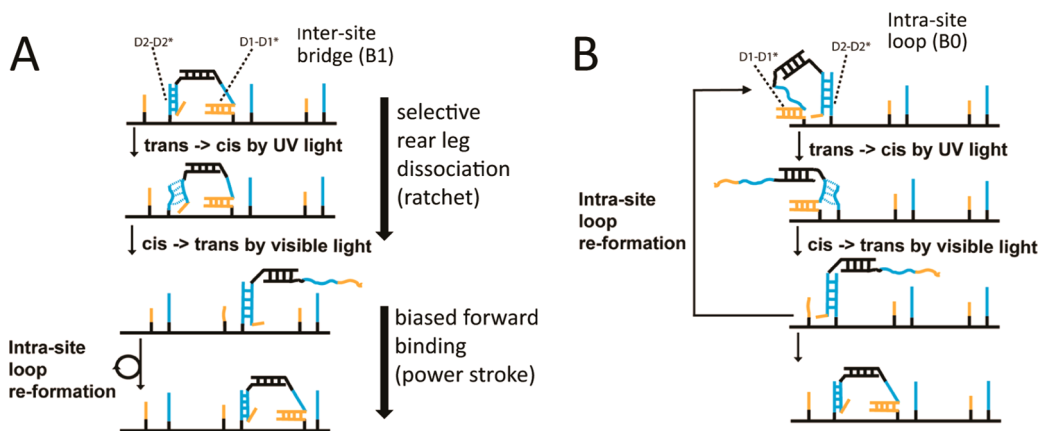

Figure 3. Stepping pattern of the motor. Shown are the major intermediate states and transition pathways for the light-driven motor starting from an intersite bridge state (A) and from an intrasite loop state (B).
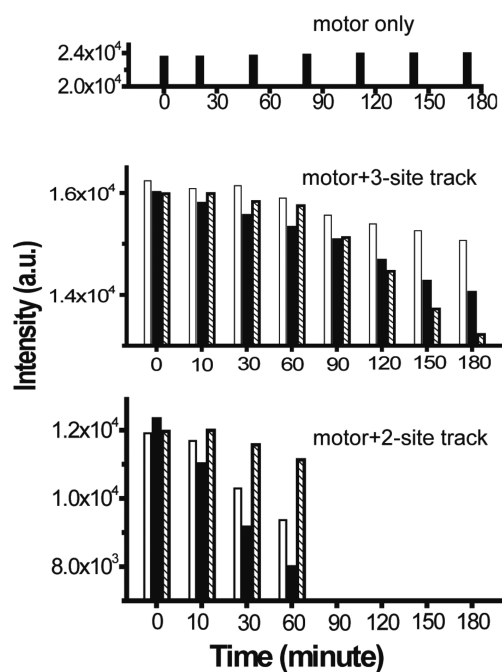
Figure 4. Motor motility. The data were obtained from the motor−track system and dye−quencher labeling illustrated in Figure 1. The three panels show the fluorescence data from three sets of experiments that used the same amount of motor sample in an equimolar motor−track mix but for different tracks as indicated. The data for zero time are from the equilibrated sample before the operation. Seven rounds of UV irradiation were applied, which lasted 10, 20, 30, 30, 30, 30, and 30 min, each followed by 20 s of visible irradiation, during which the fluorescence was collected. The fluorescence signals shown here were obtained by integrating the fluorescence spectra over the wavelength range 433−627 nm. The empty, black, and patterned bars in the middle and lower panels represent three repeats of the experiments, which each used a newly prepared motor−track sample.

motor−track mix was incubated for a long time to ensure thermodynamic equilibration. The light operation of the motor was done with seven rounds of UV irradiation that lasted 10−30 min, each followed by 20 s of visible irradiation, during which the fluorescence was collected. The control experiment was done using the motor sample alone under the same light operation. The two motility experiments were both repeated three times; each repeat was done using a newly prepared motor−track sample.

Figure 4 summarizes the fluorescence data from the motility experiments and the control experiment. A trend of successive drop of fluorescence is observed for each repeat of the two motility experiments, while the control experiment with the motor alone yielded virtually flat signals. The control experiment suggests negligible photobleaching of the dye throughout the experiments. Hence the fluorescence drop seen in the two motility experiments reflects the motor's light-driven motility toward the plus end of the track.

Intrasite Loop State. The preoperation signal from the equilibrated sample (*i.e.*, the data at time zero in

Figure 4) is 51.1% or 68.1% after the average over the repeats, for the two-site and three-site tracks, respectively, of the signal from the same amount of motors in the absence of tracks. The two ratios are close to 1/2 and 2/3 for two-site and three-site tracks, implying the existence of an intrasite loop state (*e.g.*, B0 state in Figure 4) in which a motor's two legs hybridize with D1* and D2* within a binding site. The conclusion can be drawn from the preoperation data by a rigorous analysis as below.

The preoperation fluorescence of an equimolar mix of motors and two-site tracks is

$$
\begin{aligned}
I_{\mathrm{M+T2}}(t = 0) \\
= P_{\mathrm{Loop}} \times 2 + P_{\mathrm{Loop}} \\
\times (2 - \gamma_1 - \gamma_2) + P_{\mathrm{Bridge}} \times (2 - \gamma^*) \quad (3)
\end{aligned}
$$

Here P_{Bridge} and P_{Loop} are populations for all intersite bridge states and for the loop state. γ_1 and γ_2 are the percentage of fluorescence quenched for a dye-carrying leg when it is hybridized with the D2* or D1* foothold at the track's plus end; γ^* is the average quenching percentage for the plus-end-bound leg of a motor in all possible bridge states. Since fluorescence of the equal-mole motors without the track is $I_{\mathrm{M}}(0) = P_{\mathrm{Loop}} \times 2 + P_{\mathrm{Loop}} \times 2 + P_{\mathrm{Bridge}} \times 2$, the ratio of the motor−track sample over the motor sample is

$$
\begin{aligned}
\eta_2 &= I_{\mathrm{M+T2}}(t = 0)/I_{\mathrm{M}}(t = 0) \\
&= \frac{4 - \gamma_1 - \gamma_2 + \alpha(2 - \gamma^*)}{4 + 2\alpha} \quad (4)
\end{aligned}
$$

Here $\alpha = P_{\mathrm{Bridge}}/P_{\mathrm{Loop}}$ is the population ratio of bridge states over the loop state in an equilibrated motor−track binding.

Similarly, the preoperation fluorescence of an equimolar mix of motors and three-site tracks is

$$
\begin{aligned}
I_{\mathrm{M+T3}}(t = 0) \\
= 2 \times P_{\mathrm{Loop}} \times 2 + P_{\mathrm{Bridge}} \times 2 + P_{\mathrm{Loop}} \\
\times (2 - \gamma_1 - \gamma_2) + P_{\mathrm{Bridge}} \times (2 - \gamma^*) \quad (5)
\end{aligned}
$$

In this case, the fluorescence of the equal-mole motors without the track is $I_{\mathrm{M}}(0) = P_{\mathrm{Loop}} \times 2 + P_{\mathrm{Loop}} \times 2 + P_{\mathrm{Loop}} \times 2 + P_{\mathrm{Bridge}} \times 2 + P_{\mathrm{Bridge}} \times 2$, yielding the ratio of the motor−track sample over the motor sample as

$$
\begin{aligned}
\eta_3 &= I_{\mathrm{M+T3}}(t = 0)/I_{\mathrm{M}}(t = 0) \\
&= \frac{6 - \gamma_1 - \gamma_2 + \alpha(4 - \gamma^*)}{6 + 4\alpha} \quad (6)
\end{aligned}
$$

The quenching efficiency γ_1, γ_2, and γ^* in eqs 4 and 6 can be accounted for by a single parameter: $x = \gamma_1 + \gamma_2 + \alpha\gamma^*$. Combining the two equations readily cancels x to yield

$$
\alpha = \frac{1 + 2\eta_2 - 3\eta_3}{2\eta_3 - \eta_2 - 1} \quad (7)
$$

According to eq 7, the quenching details of leg-carried dyes by the quencher may affect both η_2 and
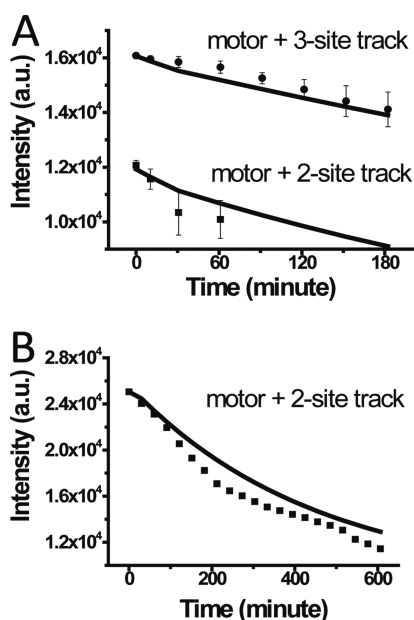
Figure 5. Motility experiments *versus* kinetic model for the motor−track system and dye−quencher labeling illustrated in Figure 1. The squares in A are fluorescence data obtained by averaging the three repeats of motility experiments shown in the middle and lower panels of Figure 4. The squares in B are the motility data for a 10 h operation in which a UV duration of 20 min was used per round of light operation. The lines are predictions of the kinetic model using the parameters from Table 1.

η_3, but the effects are canceled in the bridge-overloop population ratio α. Hence the data $\eta_2 = 0.511$ and $\eta_3 = 0.681$ yield the population ratio $\alpha = 0.138$, indicating a nontrivial presence of the loop state.

As illustrated in Figure 3B, the loop state is asymmetric also: the trailing leg is in the D1−D1* helix and the leading leg in D2−D2*. The UV irradiation selectively dissociates the leading leg, but the freed D2* foothold is occupied again *via* the downhill migration of the trailing leg under visible irradiation. The dissociated leg either binds forward to form a bridge state or binds backward with the D1 foothold to form a loop again at the same site. The backward binding makes a futile step, while the forward binding returns the motor to the forward stepping pathway. The loop formation does not compromise the motor's direction, but competes with the motor's power stroke and reduces the motor's speed. This partially explains the motor's slow motion found in the motility experiments (Figure 4). Besides, the loop may form repeatedly at the plus-end site under rounds of light operation, effectively preventing a forward-moving motor from falling off the track's end. This rationalizes the observation of over 50% fluorescence drop in a 10 h motility experiment using two-site tracks (Figure 5).

Motor Variations. The two elongated motors plus the normal one were tested in two-color motility experiments using a new motor−track design and a new dye−quencher labeling scheme (Figure 6A). To expose

more details of the motor's operation, we used a longer visible irradiation (2−10 min) and a new light source of higher irradiation intensity (∼30 times the intensity for the previous single-color motility experiments). The new motility experiments were done again using long-incubated equimolar motor−track samples and were each accompanied by a control experiment in which the same light operation was applied to the same amount of motor sample alone. The stronger irradiation resulted in a slight photobleaching in the control experiments. Influence of the photobleaching is removed from the fluorescence data of a motility experiment by dividing the data by the fluorescence data from the corresponding control experiment. The control-calibrated data are shown and further analyzed in Figure 6 and Figure 7.

The application of a stronger light source and a longer visible irradiation exposes a zigzag pattern for the fluorescence from dye labeled at both the plus-end and minus-end sites, as can be clearly seen for a motility experiment on a two-site track (Figure 6B). The fluorescence signals rise after each UV irradiation and drop over the course of ensuing visible irradiation. The rise indicates the UV-induced leg dissociation, and the drop indicates the subsequent leg−track binding under visible light.

In the two-color motility experiments, the motor's directional motion from the minus end to the plus end can be quantified by the percentage fluorescence change of the minus-end dye against its preoperation signal (*e.g.*, the data at time zero of Figure 6B) after the operational cycles minus the thus-defined percentage change of the plus-end dye. The sum of both percentages likewise quantifies the level of leg dissociation during the motor's operation. The signal of directional motion increases with successive irradiation cycles for all three motors (Figure 6C). A comparison of the motors under the same irradiation cycles shows that the signal drops in magnitude from the normal motor to the longer variation and further to the longest one (Figure 6C). The observation of poorer directional motion for longer motors is consistent with the prediction of deteriorating symmetry breaking by motor elongation, which is a character of the motor design principle.

The signal of leg dissociation from the above-mentioned percentages increases within the first one or two irradiation cycles and becomes flat afterward (Figure 6D). The saturation behavior indicates a low chance for the entire motor to derail off the track during successive irradiation cycles. Nevertheless, the elongated motors yield a higher dissociation signal than the normal motor. The observation is again compatible with deteriorating symmetry breaking by elongated motors as they access more bridge states to have less selectivity in UV-induced leg dissociation (hence more dissociation).
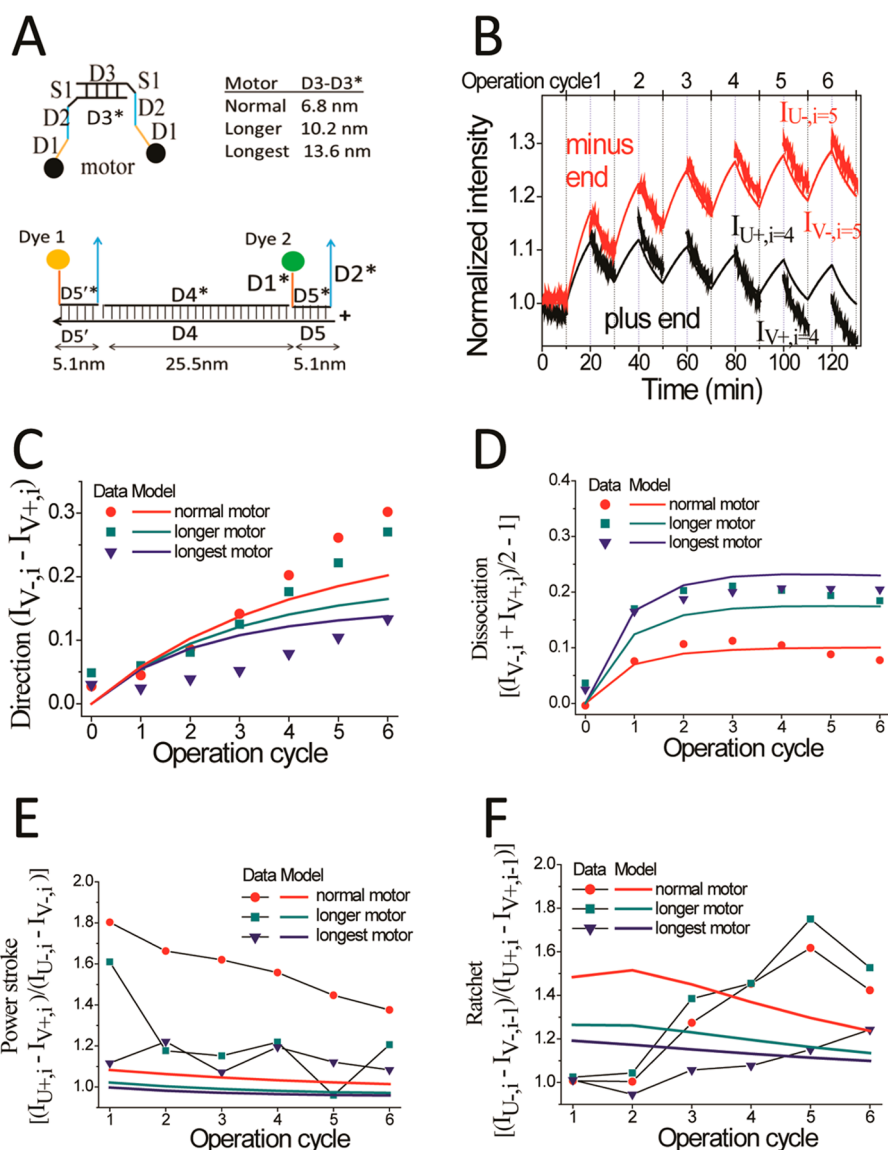
Figure 6. Motor variations (A) and two-color motility experiments (B−F). (A) The normal motor and two variations (with a longer D3−D3* duplex as indicated) are labeled with quenchers (BHQ-2, marked by black spheres), and a two-site track is labeled with two dyes at the minus and plus ends (TAMRA and FAM, marked by yellow and green spheres, respectively). **(B−F)** Operation of the three motors on the two-site track under six operation cycles of 10 min UV irradiation followed by 10 min visible light per cycle. The experiments are done using equilibrated, equimolar motor−track mix, and a half cycle of visible irradiation is applied before the first full cycle. Panel B shows typical fluorescence data (for the normal motor), which yield signals for direction (panel C), leg dissociation (D), power stroke (E), and ratchet (F). The bold curves (panel B) and symbols (C−F) are experimental data; the thin lines are predictions of the kinetic model using parameters from Table 2. The notations $I_{U+,i}$ and $I_{V+,i}$ indicate the plus-end fluorescence immediately after the UV or visible irradiation of ith operation cycle; $I_{U−,i}$ and $I_{V−,i}$ are the same except for the minus-end fluorescence.

Ratchet and Power Stroke. The zigzag patterns of fluorescence data yield signals for biased forward binding and selective rear leg dissociation. During visible irradiation, the ratio of the percentage fluorescence drop of the plus-end dye (against the preoperation fluorescence) over the percentage drop of the minus-end dye is an indicator of possible imbalance in forward and backward leg binding. The higher the ratio, the more bias for forward binding over backward binding. Similarly, the ratio of the percentage fluorescence rise of the minus-end dye (against the preoperation fluorescence) by UV irradiation over the

percentage drop of the minus-end dye is an indicator of possible imbalance in rear or front leg dissociation. The higher the ratio, the more preference for dissociation of the rear leg over the front leg. Under the same irradiation cycles, the three motors operating on the same two-site track show three features in their ratchet and power stroke signals (Figure 6E,F).

First, both the ratchet and power stroke signals tend to be lower for a longer motor, an observation compatible with the deteriorating symmetry breaking by motor elongation. Accessibility of more bridge states to a long motor tends to reduce its dissociation
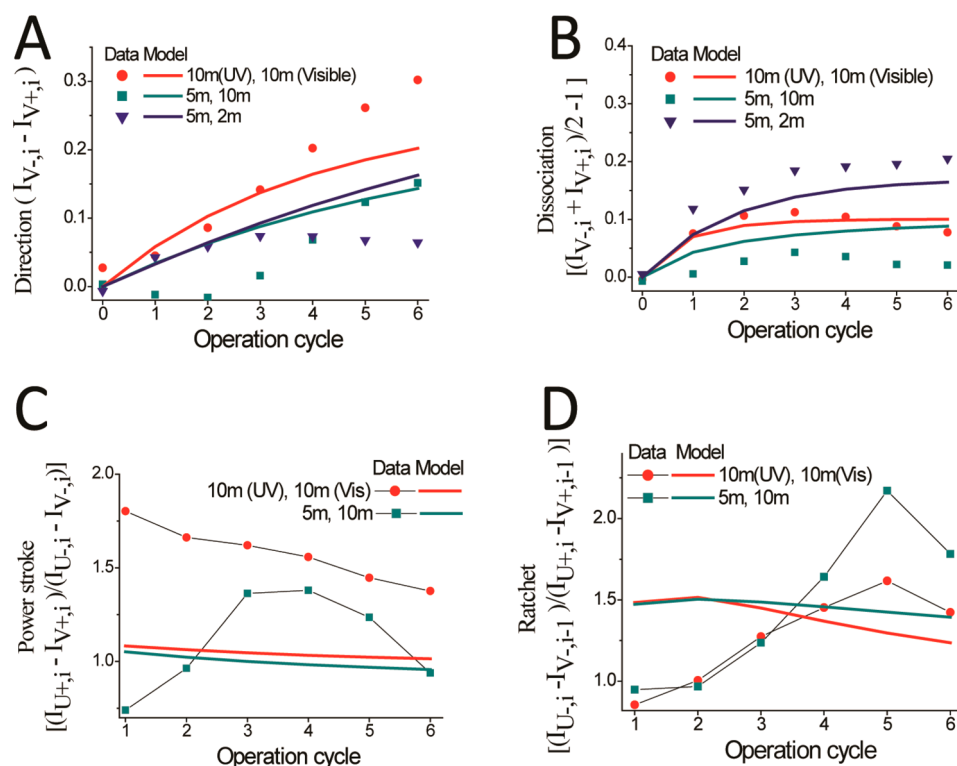
Figure 7. Operational variations for the same motor–track system and two-color motility experiments as for Figure 6. The data were obtained for the normal motor for operation cycles of different UV and visible irradiation duration as indicated. The symbols are data and the lines are predictions of the kinetic model using parameters listed in Table 2.

selectivity as mentioned above. The forward bias tends to be reduced too if a motor is long enough to reach the back site anyway from a postmigration single-leg binding.

Second, the power stroke signal drops with successive irradiation cycles, especially for the normal motor that exhibits the highest power stroke signal. This feature is in line with the expectation that the signal for unbalanced forward and backward binding comes from the operation-induced transitions from the loop state at the plus-end or minus-end site to intersite bridge states. The loop population diminishes at the minus end by successive irradiation cycles, rationalizing the trend of the power stroke signal.

Third, the ratchet signal rises within the first few irradiation cycles and drops afterward. This is compatible with the expectation that the signal for unbalanced leg dissociation comes from the UV-induced transitions from bridge states to a single-leg state at the plus-end or minus-end site. The loop-to-bridge transitions by the early irradiation cycles tend to increase the bridge population, but more operation cycles later may transfer the bridge population to a loop at the plus end. Hence the bridge population first rises and then drops, rationalizing the trend of the ratchet signal.

The dissociation rate ratio of the rear leg to the front leg can be estimated from the ratchet signal. The probability for a site to be occupied by a motor leg, P,

is linked to the fluorescence from the dye at the site l as $P = [1 - l/l_0]/\gamma$ in which l_0 is the fluorescence prior to the leg binding (i.e., from control experiments) and γ is the quenching efficiency. The average rate for leg dissociation from the start of a UV irradiation t_1 to its end at a later time t_2 is $k_d = [P(t_1) - P(t_2)]/(t_2 - t_1) = [l(t_2) - l(t_1)]/l_0\gamma(t_2 - t_1)$. The rate ratio is $k_{d-}/k_{d+} = \alpha[l_-(t_2)/l_-(0) - l_-(t_1)/l_-(0)]/[l_+(t_2)/l_+(0) - l_+(t_1)/l_+(0)]$, in which $+$ or $-$ marks the plus-end or minus-end site, $\alpha = [l_-(0)/l_{0-}\gamma_-]/[l_+(0)/l_{0+}\gamma_+]$, and the term after α is just the ratchet signal shown in Figure 6F. Since the quenching efficiency at either site is close to 100% due to the contact quenching,[50] $\gamma_-/\gamma_+ \approx 1$ and $\alpha \approx [l_-(0)/l_{0-}]/[l_+(0)/l_{0+}]$. The time-zero fluorescence for the motility experiments and corresponding control experiments yield the same value of $\alpha \approx 0.73$ for the three motors. Hence k_{d-}/k_{d+} is more than 1 for any ratchet signal above 1.37. The data in Figure 6E show that the preferential rear leg dissociation (namely, $k_{d-}/k_{d+} > 1$) exists for the normal motor (and also for the motor variation with a 10.2 nm long D3–D3* duplex).

Similarly, the rate ratio of leg binding to the front and back sites can be estimated from the power stroke signal. The average rate for leg binding from the start of a visible irradiation t_1 to its end t_2 is $k_{b\pm} = [P_\pm(t_2) - P_\pm(t_1)]/(t_2 - t_1) = [l_\pm(0) - l_\pm(t)]/l_{0\pm}\gamma_\pm(t_2 - t_1)$. The rate ratio is $k_{b+}/k_{b-} = \alpha^{-1}[l_+(t_1)/l_+(0) - l_+(t_2)/l_+(0)]/[l_-(t_1)/l_-(0) - l_-(t_2)/l_-(0)]$, with the term after α as the power stroke signal shown in Figure 6E. Since α is less than

TABLE 2. Rates and Energies for the Best Fit to the Motility Experiments in Figure 6 and Figure 7

	D1—D1* breaking	D2—D2* breaking (visible light)	D2—D2* breaking (UV light)	migration (visible light)	migration (UV light)
transition rate (s^{-1})	2.0×10^{-4}	7.0×10^{-5}	4.5×10^{-4}	0.05	6.0×10^{-5}
single-strand stretching energy (k_BT)	states 6, 7	state 8	state 9	state 10	state 11
normal motor	5.5	6.0	7.0	7.0	7.0
longer motor	5.5	6.0	6.0	6.0	7.0
longest motor	5.5	6.0	5.5	5.5	7.0
hybridization energy (k_BT)	D1—D1*	D2—D2* (visible light)		D2—D2* (UV light)	
	—7.0	—8.0		—4.0	

TABLE 1. Rates and Energies for the Best Fit to the Motility Experiments in Figure 5

	D1—D1* breaking	D2—D2* breaking (visible light)	D2—D2* breaking (UV light)	migration (visible light)	migration (UV light)
transition rate (s^{-1})	2.4×10^{-5}	4.0×10^{-6}	0.005	10	6.0×10^{-4}
single-strand stretching energy (k_BT)	states 6, 7	state 8	state 9	state 10	state 11
	0	2.0	15	15	20
hybridization energy (k_BT)	D1—D1*	D2—D2* (visible light)		D2—D2* (UV light)	
	—10 k_BT	—14 k_BT		1.0 k_BT	

1, k_{b+}/k_{b-} is more than 1 for any power stroke signal above 1. The data in Figure 6E indicate the existence of preferential forward binding (namely, $k_{b+}/k_{b-} > 1$) for all three motors. Combining the rate analyses for leg binding and dissociation, we can conclude that the normal motor achieves both ratchet and power stroke.

Operational Variations. Figure 7 shows the results of two-color motility experiments on the normal motor for different UV/visible irradiation time per operation cycle. When the visible irradiation is kept as 10 min and the UV irradiation shortened from 10 min to 5 min, the signals for directional motion and leg dissociation both drop. This is understandable since the UV-induced D2—D2* breaking amounts to the driving force for the motor. The power stroke signal also decreases as the shorter UV irradiation induces less loop-to-bridge transition. The ratchet signal for later operation cycles is slightly higher for the shorter UV irradiation, since the bridge population is better preserved during the later operation cycles with shorter UV irradiation. When the UV irradiation is kept as 5 min and the visible irradiation is shortened from 10 min to 2 min, the signal for directional motion changes little, but the dissociation signal is more than doubled. This is consistent with the role of visible irradiation to stabilize leg—track binding.

Kinetic Modeling *versus* Motility Experiments. For the first motor—track design shown in Figure 1, the kinetic model well reproduces the data of multiple sets of single-color motility experiments (Figure 5). For the second motor—track design shown in Figure 6A, the associated two-color motility experiments provide more detailed data and thereby more constraints for modeling. The kinetic model captures nearly all the data ordering between the motor variations and between the operational variations (Figures 6, 7). This qualitative agreement suggests that the model largely captures the correlations discussed above among the signals of directional motion, dissociation, ratchet, and power stroke, although the quantitative agreement is rather poor. Overall, the kinetic model, and also the mechanical model, is a useful tool for a qualitative check of consistence of the experimental data, but far from adequate for quantitative prediction. Therefore, we draw any conclusion only from experimental data throughout this study.

The model—experiment comparison reflects the challenge of modeling dynamic DNA systems that are cyclically driven through multiple states. A major difficulty comes from nonspecific binding. While a designed binding between a couple of DNA strands of complementary sequences is strongest, nonspecific bindings with other strands are inevitable since there are only four types of bases (A, G, C, T) and the sequence-encoded binding specificity is fairly poor. The nonspecific interactions, though not necessarily detectable in equilibrated DNA systems, can occur transiently in a driven system to affect its operation. The nonspecific interactions modify energies of designed states in a way that is sensitive to atomic details of a motor—track design. This partially rationalizes the rather big change of fitting parameters for the two motor—track designs (Tables 1, 2).

DISCUSSION

Brownian Ratchet and Power Stroke Contribute Additively to Motor Performance. The position-selective dissociation of the rear leg is a Brownian ratchet effect: the dissociated leg might bind back to resume the D2—D2* helix, but the ensuing asymmetric bridge B1 subjects the trailing leg to UV-induced dissociation yet again. The bridge-forming backward binding produces a futile step, which is prevented by the ratchet from developing into a full backward step. The migration-induced forward bias is a power stroke, because it uses the

energy gained from forming a longer helix to actively place the dissociated leg ahead to favor a binding forward over backward. The power stroke advances a forward step at the cost of a futile one.

The power stroke and the ratchet contribute additively to the motor's performance: the stroke suppresses the chance of futile steps that waste energy and reduce the motor's speed; the ratchet prohibits backward steps that compromise the motor's direction. Therefore, integrating a ratchet-like passive control and a stroke-like active control is a key to making advanced nanomachines that perform better yet consume less energy. We notice an ongoing debate[51] on suitability of the term "power stroke" for molecular motors from the perspective of microscopic reversibility. In this study, we follow the conventional use of this term to denote biased forward binding. Whatever you may call it, it is an extra effect different from but complementary to the ratchet effect (*i.e.*, selective dissociation). As far as the motors of this study are concerned, the two effects are linked to different experimental signals, which have been separately obtained from the zigzag patterns of two-color motility experiments.

Both Ratchet and Power Stroke Can Be Implemented *via* a Design Principle of Mechanics-Mediated Symmetry Breaking. The ratchet and stroke share the same mechanistic root in the design of a distinct free-energy hierarchy for motor−track intersite binding states, which are intermediate states for a motor's motion down the track. The ratchet originates from asymmetry breaking, namely, dominance of the asymmetric state B1 in a motor's intersite binding, which is ensured by this state attaining the lowest free energy among all possible intersite bridge states. The power stroke involves different free-energy gaps associated with forward and backward binding of the dissociated leg of a postmigration motor: The forward binding forms the lowest energy bridge B1 and hence stretches the motor least; the backward binding must form a high-energy bridge (*i.e.*, B3 or B4) and stretch the motor more. Hence the power stroke originates from the symmetry breaking also. The close relation of the symmetry breaking with the ratchet/stroke is compatible with the multiple correlations observed between the signals of directional motion, ratchet and power stroke.

A major character of the motor design principle in this study is that the symmetry breaking is caused by tuning the motor's size. Such a mechanics-mediated symmetry breaking can be clarified by considering the limit of a long motor whose single-stranded segments

are mechanically relaxed in the two reversely asymmetric bridge states B1 and B4. The free energy for either state is then dominated by the leg−track helix formation, which is identical for both states. Hence the free energies of the twin states converge to the same value in the long-motor limit, rendering the overall motor−track intersite binding symmetric. The two symmetric bridge states B2 and B3 cannot produce any selective dissociation (*i.e.*, ratchet) anyway under the UV irradiation; neither can the two reversely asymmetric states because they occur by equal chance according to Boltzmann's law so that the selective dissociation from one state is perfectly canceled by that from the other. A short motor deviating from the long-motor limit must be stretched in the two states to affect their free energies. A free-energy gap then arises between the twin states because their reversed asymmetry requires different stretch of the motor. Consequently, the asymmetric B1 becomes the single, lowest lying bridge, breaking the motor−track intersite binding symmetry. The size dependence of the symmetry breaking is confirmed by the experiments of the normal motor *versus* the two elongated motor variations.

The design principle[31] for the present motors was derived from biological nanomotors kinesin[30] and myosin V.[49] The two biomotors and the present artificial motors are all symmetric bipeds on tracks of identical binding sites that each host an internal, local asymmetry. As this study suggests, such a highly symmetric motor−track system attains a direction not necessarily by burn-the-bridge methods;[11−13,15] instead the direction can be produced by a mechanics-mediated symmetry that amplifies the intrasite asymmetry into intersite ratchet and power stroke.

CONCLUSION

A light-powered DNA nanomotor and new variations are systematically studied using different fluorescence labeling schemes and light operations. The experimental data suggest that the motor achieves a ratchet-plus-power stroke synergic control through a mechanics-mediated symmetry breaking, in a way similar to biological nanomotors. This study presents an experimental validation for the bioinspired design principle of mechanical breaking of symmetry for integrated passive−active control. Using the rationally designed DNA motors as a model system and augmenting the data with mechanical and kinetic modeling, this study provides valuable mechanistic insights that may help advance molecular control in future nanotechnological systems.

MATERIALS AND METHODS

Motor−Track Fabrication. The motor−track systems shown in Figure 1 were fabricated previously[20] using a stepwise

self-assembly method. Details of the fabrication method and the nucleotide sequences for the DNA strands forming the motor (MS1 and MS2) and the track (major strands TS1, TS2 and

three end strands ES1, ES2, ES3; see Figure 1) can be found in ref 20. The two elongated motor variations contain in their D3 and complementary D3* segments extra nucleotide sequences, which are 5′-GGGGATTTCG or 5′-ATGTCGGGGATTTCGTCACA from the 3′ end of D3 of the normal motor. In addition, the motors now carry two quenchers (BHQ-2) at their legs, and the track is redesigned to carry two different dyes (FAM and TAMRA with excitation/emission wavelengths of 559 nm/583 nm) at the plus and minus ends (Figure 6A). For the site-specific labeling, the D5 segment at the minus-end site is mutated into a new sequence D5′ (5′-CGAACATTGCTGTTG-3′). The new motors and a two-site track with the two-dye labeling are fabricated using the self-assembly method. Since the track contains only four DNA strands (a template strand hybridized with three short strands; see Figure 6A), it is formed by a one-step assembly and is confirmed by a single band of expected molecular weight using polyacrylamide gel electrophoresis (PAGE).

Fluorescence Detection of Motor Motility. The motor's light-driven motility was detected using a fluorescence method. An equimolar mix of the motor and track sample was incubated over a long time (24 h) to ensure thermodynamic equilibration of the motor−track binding. The incubated sample was then used for light operation and fluorescence measurement. The motility experiments were conducted using a Cary Eclipse spectrophotometer (Varian, Inc.) equipped with a 100 W xenon flash lamp (Agilent Technologies, 0.1 s per flash). For each round of irradiation operation, a walker−track sample was first irradiated by UV light through a filter of narrow wavelength window (350 nm−380 nm) for a period of time, followed by visible irradiation ($\lambda > 400$ nm) and fluorescence measurement. The filtered UV flash has a low power (∼10 microwatts as measured by a power meter), effectively suppressing photobleaching of the dye-labeled sample. The motility experiments were all done at 25 °C for submicromolar concentrations in a working volume of ∼600 μL. The low concentrations suppress the possibility of one motor cross-linking more than one track.

Simplistic Mechanical Model. In the mechanical model, we estimate the free energy for a motor−track state as the leg−track hybridization energy associated with the helix formation plus the stretching energy of the remaining single-stranded component of the motor. Any other nonspecific motor−track interactions are ignored, which is a rather crude approximation. The hybridization energies for helices D1−D1* and D2−D2* are estimated as −6.65 and −24.7 kcal/mol (25 °C) for the sequences adopted in this study using the nearest-neighbor thermodynamics[52] for DNA. The strand-stretching energy is estimated using a worm-like chain formula:[30] $F(l,d) = (k_BT)(l/l_p) [x^2(3-2x)/4(1-x)]$. Here T is the temperature in Kelvin, $x = d/l$, l is the total contour length of the single-stranded portion of the motor (∼0.7 nm per nucleotide from ref 53), and d is the extension required of the single-stranded portion to form the motor−track binding state. l_p is the persistence length for single-stranded DNA (1−3 nm from ref 54).

Kinetic Model. A kinetic model for the DNA motor is constructed as a tool for a consistence check of the experimental data. The motor's kinetics is modeled as a network of transitions between possible motor−track binding states, which are intersite bridge states B1 and B2, single-site binding states, and the fully derailed state. These states are enumerated and schematically illustrated in Figure 8. In the single-site binding states, one leg of the motor is dissociated, but the other may be bound to the track *via* the D2−D2* helix or D1−D1* helix or *via* both helices to form an intrasite loop (termed B0 state).

The motor's stepping under the optical operation is computed by solving the time-dependent master equation

$$\frac{dp_i(t)}{dt} = \sum_{j \neq i} k_{ji}(t)\, p_j(t) - \sum_{i \neq j} k_{ij}(t)\, p_i(t) \qquad (1)$$

Here p_i is the normalized population of the ith state ($\sum p_i = 1$), and k_{ij} the transition rate from the ith to the jth state.

The time-dependent fluorescence of the motor−track sample is estimated by counting the populations that are subject to the quenching effect. For a motor on a two-site track by the first labeling scheme (Figure 1), the time-dependent fluoresecnce
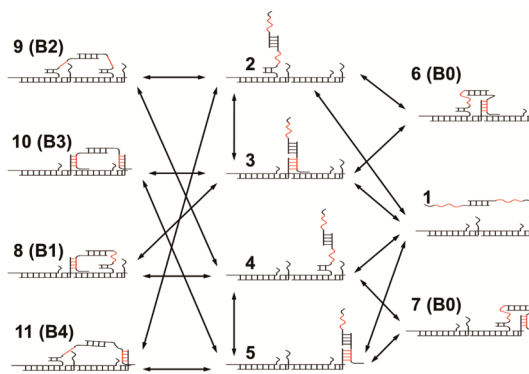

Figure 8. Motor−track binding states. Shown here are the possible states for a track with two composite binding sites, including one fully derailed state (state 1), four single-leg binding states (states 2−5), two loop states (states 6, 7), and four two-leg bridge states (states 8−11). Seven more states are possible for a three-site track, including single-leg and loop states at the middle site and two-leg states between the middle and minus-end sites. The azo-carrying strands of the motor are highlighted in red, and the transitions are marked by arrows.

is counted as

$$
\begin{aligned}
I(t) = {} & \frac{I_{control}}{2} \\
& \times \{2 - p_7(t)(\gamma_1 + \gamma_2) - \gamma_1[p_5(t) + p_{10}(t) + p_{11}(t)] - \gamma_2 \\
& \times [p_4(t) + p_8(t) + p_9(t)]\}
\end{aligned}
$$

$$(2)$$

$I_{control}$ is the fluorescence intensity of the motor sample without the track as measured in the control experiment. γ_1 is the percentage of fluorescence quenched for a dye-carrying leg when it is hybridized with the D2* foothold at the track's plus end, and γ_2 is the percentage of fluorescence quenched for a leg hybridized with the D1* at the plus end. The factor of 2 in the above equation accounts for the presence of two dyes on the motor. Similar equations are readily available for the three-site track and for the second labeling scheme (Figure 6A).

The quenching efficiency γ_1 may be reasonably assumed as 100% because the dye−quencher proximity for a D2*-hybridized leg at the plus end allows for contact quenching, and near 100% efficiency is previously reported for quencher IBRQ in contact quenching (see Table S2 of ref 55). In addition, a ∼89% quenching for the dye FAM over a dye−quencher separation of ∼3 nm is previously observed for the BHQ-2 quencher (see Table 1 of ref 50). A similar level of quenching efficiency is expected for γ_2 because IBRQ and BHQ-2 have a similar spectrum overlap with FAM dye and because a D1*-hybridized leg at the plus end has a similar dye−quencher separation. Hence we take $\gamma_2 = 100\%$ also for a crude approximation for the kinetic model. For the second labeling scheme (Figure 6A), a dye at D1* is contact quenched by D1−D1* hybridization and a 100% quenching efficiency is assumed. The dye is also quenched effectively by a nearby D2−D2* hybridization for the same reason as for γ_2 in the first labeling scheme, and a 100% quenching efficiency is assumed also for a crude approximation.

The initial populations for the various states satisfy the Boltzmann distribution since the motility experiments are started from an equilibrated motor−track sample. Hence the population ratio between state i and state j is $p_i(t=0)/p_j(t=0) = \exp(-\Delta E_{ij}/k_BT)$ with ΔE_{ij} being the free-energy gap between the states ($\Delta E_{ij} = E_i - E_j$). The transition rates are also constrained[56,57] by free-energy gaps between states, namely, $k_{ij}/k_{ji} = \exp(\Delta E_{ij}/k_BT)$. Following the mechanical model, the free energy for a motor−track state is counted from the leg−track hybridization energy and the strand-stretching energy, which are not taken from the simplistic mechanical model but used as fitting parameters for the kinetic model. The above

thermodynamic considerations reduce the number of free rates to five, which were used as fitting parameters. Since a constant intensity for the UV or visible irradiation is used in a motility experiment, the breaking/formation of D2−D2* helices were characterized by single rates in the kinetic model. Without any UV irradiation, an equilibrated motor−track system satisfies microscopic reversibility. This requirement is satisfied by the kinetic model, as it predicts flat fluorescence signals by assigning zero values for UV-induced transitions.

Conflict of Interest: The authors declare no competing financial interest.

REFERENCES AND NOTES

1. Anelli, P. L.; Spencer, N.; Stoddart, J. F. A Molecular Shuttle. *J. Am. Chem. Soc.* **1991**, *113*, 5131.
2. Murakami, H.; Kawabuchi, A.; Kotoo, K.; Kunitake, M.; Nakashima, N. A Light-Driven Molecular Shuttle Based on a Rotaxane. *J. Am. Chem. Soc.* **1997**, *119*, 7605–7606.
3. Brouwer, A. M.; Frochot, C.; Gatti, F. G.; Leigh, D. A.; Mottier, L.; Paolucci, F.; Roffia, S.; Wurpel, G. W. H. Photoinduction of Fast, Reversible Translational Motion in a Hydrogen-Bonded Molecular Shuttle. *Science* **2001**, *291*, 2124–2128.
4. Balzani, V.; Clemente-Leon, M.; Credi, A.; Ferrer, B.; Venturi, M.; Flood, A. H.; Stoddart, J. F. Autonomous Artificial Nanomotor Powered by Sunlight. *Proc. Natl. Acad. Sci. U.S.A.* **2006**, *103*, 1178–1183.
5. Koumura, N.; Zijlstra, R. W. J.; van Delden, R. A.; Harada, N.; Feringa, B. L. Light-Driven Monodirectional Molecular Rotor. *Nature* **1999**, *401*, 152–155.
6. Kelly, T. R.; Silva, H. D.; Silva, R. A. Unidirectional Rotary Motion in a Molecular System. *Nature* **1999**, *401*, 150–152.
7. Hernandez, J. V.; Kay, E. R.; Leigh, D. A. A Reversible Synthetic Rotary Molecular Motor. *Science* **2004**, *306*, 1532–1536.
8. Fletcher, S. P.; Dumer, F.; Pollard, M. M.; Feringa, B. L. A Reversible, Unidirectional Molecular Rotary Motor Driven by Chemical Energy. *Science* **2005**, *310*, 80–82.
9. Sherman, W. B.; Seeman, N. C. A Precisely Controllable DNA Biped Walking Devices. *Nano Lett.* **2004**, *4*, 1203–1207.
10. Shin, J. S.; Pierce, N. A. A Synthetic DNA Walker for Molecular Transport. *J. Am. Chem. Soc.* **2004**, *126*, 10834–10835.
11. Yin, P.; Yan, H.; Daniell, X. G.; Tuerberfield, A. J.; Reif, J. H. A Unidirectional DNA Walker That Moves Autonomously along a Track. *Angew. Chem., Int. Ed.* **2004**, *43*, 4906–4911.
12. Bath, J.; Green, S. J.; Turberfield, A. J. A Free-Running DNA Motor Powered by a Nicking Enzyme. *Angew. Chem., Int. Ed.* **2005**, *44*, 4358–4361.
13. Tian, Y.; He, Y.; Chen, Y.; Yin, P.; Mao, C. A DNAzyme That Walks Processively and Autonomously along a One-Dimensional Track. *Angew. Chem., Int. Ed.* **2005**, *44*, 4355–4358.
14. Green, S. J.; Bath, J.; Turberfield, A. J. Coordinated Chemomechanical Cycles: A Mechanism for Autonomous Molecular Motion. *Phys. Rev. Lett.* **2008**, *101*), 1–4.
15. Omabegho, T.; Sha, R.; Seeman, N. C. A Bipedal DNA Brownian Motor with Coordinated Legs. *Science* **2009**, *324*, 67–71.
16. Bath, J.; Green, S. J.; Allen, K. E.; Turberfield, A. J. Mechanism for a Directional, Processive, and Reversible DNA Motor. *Small* **2009**, *5*, 1513–1516.
17. von Delius, M.; Geertsema, E. M.; Leigh, D. A. A Synthetic Small Molecule That Can Walk Down a Track. *Nat. Chem.* **2009**, *2*, 96–101.
18. Wickham, S. F. J.; Endo, M.; Katsuda, Y.; Hidaka, K.; Bath, J.; Sugiyama, H.; Turberfield, A. J. Direct Observation of Stepwise Movement of a Synthetic Molecular Transporter. *Nat. Nanotechnol.* **2011**, *6*, 166–169.
19. You, M.; Chen, Y.; Zhang, X.; Liu, H.; Wang, R.; Wang, K.; Williams, K. R.; Tan, W. An Autonomous and Controllable Light-Driven DNA Walking Device. *Angew. Chem., Int. Ed.* **2012**, *51*, 2457–2460.
20. Cheng, J.; Sreelatha, S.; Hou, R. Z.; Efremov, A.; Liu, R. C.; van der Maarel, J. R.; Wang, Z. S. Bipedal Nanowalker by Pure Physical Mechanisms. *Phys. Rev. Lett.* **2012**, *109*, 238104.
21. Gu, H.; Chao, J.; Xiao, S. J.; Seeman, N. C. A Proximity-Based Programmable DNA Nanoscale Assembly Line. *Nature* **2010**, *465*, 202–206.
22. Lund, K.; Manzo, A. J.; Dabby, N.; Michelotti, N.; Johnson-Buck, A.; Nangreave, J.; Taylor, S.; Pei, P.; Stojanovic, M. N.; Walter, N. G.; *et al.* Molecular Robots Guided by Prescriptive Landscapes. *Nature* **2010**, *465*, 206–210.
23. He, Y.; Liu, D. R. Autonomous Multistep Organic Synthesis in a Single Isothermal Solution Mediated by a DNA Walker. *Nat. Nanotechnol.* **2010**, *5*, 778–782.
24. Lewandowski, B.; De Bo, G.; Ward, J. W.; Papmeyer, M.; Kuschel, S.; Aldegunde, M. J.; Gramlich, P. M. E.; Heckmann, D.; Goldup, S. M.; D'Souza, D. M.; *et al.* Sequence-Specific Peptide Synthesis by an Artificial Small-Molecule Machine. *Science* **2013**, *339*, 189–193.
25. Tierney, H. L.; Murphy, C. J.; Jewell, A. D.; Baber, A. E.; Iski, E. V.; Khodaverdian, H. Y.; McGuire, A. F.; Klebanov, N.; Sykes, E. C. H. Experimental Demonstration of a Single-Molecule Electric Motor. *Nat. Nanotechnol.* **2011**, *6*, 625–629.
26. Astumian, R. D. Thermodynamics and Kinetics of a Brownian Motor. *Science* **1997**, *276*, 917–922.
27. Oster, G.; Wang, H. Reverse Engineering a Protein: The Mechanochemistry of ATP Synthase. *Biochim. Biophys. Acta* **2000**, *1458*, 482–510.
28. Reimann, P. Brownian Motors: Noisy Transport Far from Equilibrium. *Phys. Rep.* **2002**, *361*, 57–265.
29. Howard, J. Protein Power Strokes. *Curr. Biol.* **2006**, *16*, R517–R519.
30. Wang, Z. S.; Feng, M.; Zheng, W. W.; Fan, D. G. Kinesin Is an Evolutionarily Fine-Tuned Molecular Ratchet-and-Pawl Device of Decisively Locked Directionality. *Biophys. J.* **2007**, *93*, 3363–3372.
31. Wang, Z. S. Synergic Mechanism and Fabrication Target for Bipedal Nanomotors. *Proc. Natl. Acad. Sci. U.S.A.* **2007**, *104*, 17921–17926.
32. Gennerich, A.; Vale, R. D. Walking the Walk: How Kinesin and Dynein Coordinate Their Steps. *Curr. Opin. Cell Biol.* **2009**, *21*, 59–67.
33. Fox, R. F. Rectified Brownian Movement in Molecular and Cell Biology. *Phys. Rev.* **1998**, *E 57*, 2177–2203.
34. Vale, R. D.; Milligan, R. A. The Way Things Move: Looking under the Hood of Molecular Motor Proteins. *Science* **2000**, *288*, 88–95.
35. Mather, W. H.; Fox, R. F. Kinesin's Biased Stepping Mechanism: Amplification of Neck Linker Zippering. *Biophys. J.* **2006**, *91*, 2416–2426.
36. Efremov, A.; Wang, Z. S. Maximum Directionality and Systematic Classification of Molecular Motors. *Phys. Chem. Chem. Phys.* **2011**, *13*, 5159–5170.
37. Nishiyama, M.; Higuchi, H.; Yanagida, T. Chemomechanical Coupling of the Forward and Backward Steps of Single Kinesin Molecules. *Nat. Cell Biol.* **2002**, *4*), 790–797.
38. Carter, N. J.; Cross, R. A. Mechanics of the Kinesin Step. *Nature* **2005**, *435*), 308–312.
39. Toyabe, S.; Watanabe, T. M.; Okamoto, T.; Kudo, S.; Muneyuki, E. Thermodynamic Efficiency and Mechanochemical Coupling of F_1-ATPase. *Proc. Natl. Acad. Sci. U.S.A.* **2011**, *108*, 17951–17956.
40. Efremov, A.; Wang, Z. S. Universal Optimal Working Cycles of Molecular Motors. *Phys. Chem. Chem. Phys.* **2011**, *13*, 6223–6233.
41. Hou, R. Z.; Wang, Z. S. Role of Directional Fidelity in Multiple Extreme Performance of F1-ATPase Motor. *Phys. Rev. E* **2013**, *88*, 022703.
42. Wang, Z. S.; Hou, R. Z.; Efremov, A. Directional Fidelity of Nanoscale Motors and Particles Is Limited by the 2nd Law of Thermodynamics-*via* a Universal Equality. *J. Chem. Phys.* **2013**, *139*, 035105.

43. Yasuda, R.; Noji, H.; Kinosita, K.; Yoshida, M. F_1 ATPase Is a Highly Efficient Molecular Motor That Rotates with Discrete 120° Steps. *Cell* **1998**, *93*, 1117–1124.

44. Block, S. M. Nanometres and Piconewtons: The Macromolecular Mechanics of Kinesin. *Trends Cell Biol.* **1995**, *5*, 169–175.

45. Faucheux, L. P.; Bourdieu, L. S.; Kaplan, P. D.; Libchaber, A. J. Optical Thermal Ratchet. *Phys. Rev. Lett.* **1995**, *74*, 1504–1507.

46. Linke, H.; Humphrey, T. E.; Loefgren, A.; Sushkov, A. O.; Newbury, R.; Taylor, R. P.; Omling, P. Experimental Tunneling Ratchets. *Science* **1999**, *286*, 2314–2317.

47. Lee, S.-H.; Ladavac, K.; M, P.; Grier, D. G. Observation of Flux Reversal in a Symmetric Optical Thermal Ratchet. *Phys. Rev. Lett.* **2005**, *94*, 110601.

48. Asanuma, H.; Liang, X.; Nishioka, H.; Matsunaga, D.; Liu, M.; Komiyama, M. Synthesis of Azobenzene-Tethered DNA for Reversible Photo-Regulation of DNA Functions: Hybridation and Transcription. *Nat. Protoc.* **2007**, *2*, 203–212.

49. Xu, Y.; Wang, Z. S. Comprehensive Physical Mechanism of Two-Headed Biomotor Myosin V. *J. Chem. Phys.* **2009**, *131*), 245104.

50. Marras, S. A. E.; Kramer, F. R.; Tyagi, S. Efficiences of Fluorescence Resonance Energy Transfer and Contact-Mediated Quenching in Oligonucleotide Probes. *Nucleic Acids Res.* **2002**, *30*, e122.

51. Astumian, R. D. Thermodynamics and Kinetics of Molecular Motors. *Biophys. J.* **2010**, *98*, 2401–2409.

52. SantaLucia, J. J. A Unified View of Polymer, Dumbbell, and Oligonucleotide DNA Nearest-Neighbor Thermodynamics. *Proc. Natl. Acad. Sci. U.S.A.* **1998**, *95*, 1460–1465.

53. Murphy, M. C.; Rasnik, I.; Cheng, W.; Lohman, T. M.; Ha, T. Probing Single-Stranded DNA Conformational Flexibility Using Fluorescence Spectroscopy. *Biophys. J.* **2004**, *86*, 2530–2537.

54. Mills, J. B.; Vacano, E.; Hagerman, P. J. Flexibility of Single-Stranded DNA: Use of Gapped Duplex Helices to Determine the Persistence Lengths of Poly(dT) and Poly(dA). *J. Mol. Biol.* **1999**, *285*), 245–257.

55. You, Y.; Tataurov, A. V.; Owczarzy, R. Measuring Thermodynamic Details of DNA Hybridization Using Fluorescence. *Biopolymers* **2011**, *95*, 472–486.

56. Hill, T. L. *Free Energy Transduction and Biochemical Cycle Kinetics*; Springer: New York, 1989.

57. Liepelt, S.; Lipowsky, R. Kinesin's Network of Chemomechanical Motor Cycles. *Phys. Rev. Lett.* **2007**, *98*, 258102.